OPEN ACCESS

Challenges and Opportunities of Water-Based Processing of Prussian White Electrodes

Journal of The Electrochemical Society, 2026 **173** 160522

Challenges and Opportunities of Water-Based Processing of Prussian White Electrodes

Xuebin Wu,[1,z] Noah Keim,[1] David Burger,[2] Haofei Zhou,[2] Dhruvil Virani,[1] Marcus Müller,[1] Ulrike Kaufmann,[1] Joachim R. Binder,[1] Philip Scharfer,[2] Wilhelm Schabel,[2] Helmut Ehrenberg,[1] and Werner Bauer[1]

[1]*Institute for Applied Materials (IAM), Karlsruhe Institute of Technology (KIT), Eggenstein-Leopoldshafen, Baden-Württemberg 76344, Germany*
[2]*Thin Film Technology (TFT), Karlsruhe Institute of Technology (KIT), Eggenstein-Leopoldshafen, Baden-Württemberg 76344, Germany*

Prussian white (PW) is among the most promising cathode materials for sodium-ion batteries due to its high theoretical specific capacity and cost-effective synthesis routes. To maintain cost advantages compared with lithium-ion batteries, water-based electrode processing is desirable; however, the strong water affinity of PW introduces significant challenges. Here, we systematically investigate the influence of thermal pre-treatment of PW on particle morphology during aqueous processing and on the electrochemical performance and evaluate how binder selection affects electrode stability. Repeated dehydration and rehydration during pre-treatment and subsequent water-based processing trigger phase transformations, leading to surface cracking and porosity. In addition, direct contact with water can promote partial dissolution of Na^+ and $[Fe(CN)_6]^{4-}$ and generate vacancies within the crystal framework. Although N-methyl-2-pyrrolidone-based processing yields unwarped electrodes, high bulk and interfacial resistances limit rate capability at C/2. In contrast, the water-processed electrode delivers higher specific discharge capacity despite inward warping. An additional step of thermal pre-treatment can be beneficial for capacity retention. Overall, these findings reveal a trade-off between particle integrity and long-term electrochemical cyclability of PW electrodes and suggest that binder selection should be a key consideration in further optimization.

[DOI: 10.1149/1945-7111/ae998e]

Manuscript submitted June 22, 2026; revised manuscript received July 31, 2026. Published August 27, 2026.

The rapid growth of global energy demand and the expansion of renewable energy technologies have intensified the need for scalable and low-cost energy storage solutions. While lithium-ion batteries (LIB) have the highest market share, concerns regarding the limited availability of lithium resources, rising material costs, and associated supply chain risks have accelerated research into supplemented technologies.[1,2] Among the different possibilities, sodium ion batteries (SIB) garnered significant attention due to the high abundance and low cost of sodium.

Prussian blue analogs (PBA) are among the most promising cathode materials for SIB as they combine high theoretical capacity and a cost-effective and simple synthesis route.[1,2] A particularly interesting material is Prussian white (PW), the fully sodiated form of PBA, offering high capacities and structural channels in the crystal lattice, which favor sodium transport. Despite these advantages, further cost reduction is essential for SIB to remain competitive with lithium-ion batteries,[3] especially considering that cathode materials for lithium-ion batteries such as lithium iron phosphate (LFP) can be processed in water-based systems. Electrode manufacturing based on organic solvents like N-methyl-2-pyrrolidone (NMP) is a cost driver due to high costs of explosion protection and solvent recovery and would reduce the cost advantage of SIB in comparison.[4,5] However, water-based processing of PW electrodes poses some critical challenges, which will be explored in this work.

One major challenge related to water-based processing is the interaction between water and the active material (AM). Both layered transition metal oxide and PBA used in SIB have been reported to react with humid air and form sodium hydroxide.[6,7] This process may reduce the amount of electrochemically available Na^+ ions. In addition, the generated sodium hydroxide can dissolve in the aqueous phase during water-based processing and increase the slurry pH. At sufficiently high pH, the native protective oxide layer of aluminum can dissolve, resulting in aluminum corrosion and gas formation.[8–10]

In the case of PW, additional challenges arise due to its strong affinity to water. Residue water can be classified into three types according to its binding mechanism: (1) surface-adsorbed, (2) interstitial and (3) coordinated water, with the latter two incorporated in the crystal lattice.[11] Depending on synthesis and drying conditions, PW can contain different amounts of residue water of up to 18 wt.-% according to the chemical compositions or thermogravimetric analysis (TGA) results reported in multiple papers.[12–17] Residue water is generally undesirable as it can lead to side reactions during charge and discharge and affects the cycling stability adversely.[18] The handling of this water during electrode manufacturing raises questions about humidity management and its presence poses possibility of phase changes alongside the processing. The uptake of water into the interstitial sites or its removal induces phase transitions between monoclinic and rhombohedral lattice configuration,[14,19] leading to volume change and cracks. Therefore, correct choice of binder is essential as it strongly determines electrode stability during and after aqueous processing.

This work therefore explores both the influence of different binder systems on the quality of the final electrodes, as well as the impact of active material pre-treatment and the corresponding cell performance.

Experimental

Synthesis of Prussian white.—The Prussian white used in this work was synthesized as described by Büchele et al.[20] based on co-precipitation method in an aqueous medium. The reaction to obtain a fully sodiated Mn-PW can be expressed as:

$$Na_4\left[Fe(CN)_6\right] + MnSO_4 \rightarrow Na_2Mn\left[Fe(CN)_6\right] + Na_2SO_4.$$

The newly synthesized material was placed into a vacuum furnace (60 °C, ~50 hPa) for at least 2 d for water evaporation and then the obtained PW powder was transferred into an argon-filled glovebox (O_2 < 0.5 ppm, H_2O < 0.5 ppm). For one representative batch, the composition was quantified as $Na_{1.75}Mn[Fe(CN)_6]_{0.92}$

[z]E-mail: xuebin.wu@kit.edu

Table I. Drying conditions regarding impact of multiple phase transitions on the cathode active material.

Process step	Drying conditions		
Pre-Treatment	150 °C	15 h	$<10^{-3}$ hPa
Dispersion Drying	60 °C	15 h	∼1.5 hPa
Post-Drying	130 °C	15 h	$<10^{-3}$ hPa

· $2.4H_2O$ using inductively coupled plasma optical emission spectroscopy (ICP-OES, see Table AI) as well as TGA (see Fig. A·1). The morphology of the as-received PW particles is shown in Fig. A·2.

Influence of drying steps on PW material.—A typical process chain for wet electrode manufacturing involves multiple drying steps along the sequence of slurry mixing, coating, drying, calendaring and post-drying. As a special feature, an additional pre-treatment drying is performed in this investigation on the PW prior to slurry preparation. This sample is hereinafter referred to as D-PW, whilst the original material, without this pre-treatment, is designated H-PW. Here D and H stands for the state of PW (dehydrated and hydrated, respectively) before mixing with water, regardless of the following processing steps including dispersion drying and post-drying. The repeated hydration or drying steps will enforce various phase transitions in the PW.[14,18,19,21] This will be further discussed in Results and Discussion (see *Surface change and phase transitions of Prussian white during water-based processing*). To investigate these phase changes during the three drying steps during processing, the following drying conditions were defined and are going to be addressed accordingly in the results, see Table I.

The pre-treatment aims at removal of the interstitial water remaining from the synthesis process. To ensure that the crystal lattice water is removed from the sample, harsh drying conditions must be applied. The PW was therefore heated to 150 °C in a high vacuum ($<10^{-3}$ hPa) created by a rotary vane pump (DUO 10 M, Pfeiffer Vacuum, Germany), as suggested by Maddar et al. and Büchele et al.[20,21] Dispersion drying was performed under moderate conditions with a reduced temperature and a lower vacuum (60 °C, 1.5 hPa). Finally, the impact of post-drying, intended to prevent water from entering the cells, is reproduced at 130 °C and high vacuum ($<10^{-3}$ hPa) for 15 h. A slightly lower temperature is set compared to the pre-treatment step, as the electrodes usually contain additives with limited temperature stability.

For the dispersion investigation, a simplified composition was used, only mimicking a slurry step. The PW was dispersed in water with a PW/water mass ratio of 58:100 by means of a speed mixer (DAC 150, Hauschild Engineering, Germany) at 2000 rpm for 15 min without further additives and stored at 20 °C for 6 h.

Electrode manufacturing.—For comparison, electrodes were manufactured via water-based or NMP-based slurry routes. Slurries were prepared by using a disc agitator (Dispermat CA60, VMA Getzmann, Germany) with a 40 mm toothed disk as a stirrer and a stainless-steel dispersion container with an inner diameter of 6.5 cm and an internal height of 8.5 cm (250 ml). The rotational speed varied from 1000 rpm when carbon additives were added to up to 2000 rpm when dispersing the active material. To ensure a defined composition, Prussian white containing a defined amount of crystal water was weighed in the argon-filled glovebox before being added into the slurry. Binders used throughout this study are summarized in Table II. The pH values of the corresponding aqueous slurries are also recorded and presented in Table AII.

For the electrochemical investigations, a composition of 88.0 wt.-% PW, 3.9 wt.-% carbon black (CB, C-NERGY, Super C65, Imerys Graphite & Carbon, Switzerland), 2.0 wt.-% VGCF (vapor-grown carbon fiber, Resonac Corporation, Japan), 0.1 wt.-% SWCNT (single-walled carbon nanotube, TUBALL BATT, suspension in H_2O or in NMP, OCSiAl EUROPE, Luxembourg), and 6.0 wt.-% of a blend with binders from Table II was prepared. In case of an NMP-based slurry, 5.9 wt.-% PVDF + 0.1 wt.-% PAA was used as binder system. PAA is added to this slurry to partially neutralize the basicity of PW and slow down gelation of the PVDF because basic conditions favor defluorination of the binder.[22] Water-based slurries contain 2.0 wt.-% CMC (2000 PA, IFF Speciality Products, Germany) and 4.0 wt.-% of another water-soluble binder species. All cathode slurries had a solid content of 35 wt.-%. Coated electrodes are going to be referred to depending on the binder used. Finally, slurries were coated onto a 16 µm thick aluminum foil (TOB-A16, TOB NEW ENERGY, China for investigations on binder selection and Batte-Foil-0004 W, Pi-Kem, UK for electrochemical tests) using a doctor blade on a roll-to-roll coating line (KTFS, Mathis AG, Switzerland). The web speed of the coater was set at 0.2 m min^{-1}, with the areal loading of the electrodes set at 1.12 mAh cm^{-2} ± 0.05 mAh cm^{-2} using 160 mAh g^{-1} as specific capacity of the Prussian white. All cathodes were calendered to a density of 1.10 g cm^{-3} ± 0.05 g cm^{-3} (GLK200, Saueressig, Germany).

For the trials on the mechanical properties to substitute TRD by other water-based binders, the slurry consisted of 90.0 wt.-% PW (as received without pre-treatment), 4.0 wt.-% CB (C-NERGY, Super C65, Imerys Graphite & Carbon, Switzerland), 2.0 wt.-% of an alternative CMC (Sunrose MAC500LC, Nippon Paper Ltd. Japan) and 4.0 wt.-% of a second polymeric binder, see Table II. For the binder study, no carbon fibers or carbon nanotubes were used to stress the system regarding its cohesion and susceptibility for cracks depending on the binder used.

Cell assembly.—All cathodes and anodes were dried in a vacuum furnace attached to the glovebox (130 °C, 15 h, $< 10^{-3}$ hPa), before being placed directly into an argon-filled glovebox ($O_2 < 0.5$ ppm, $H_2O < 0.5$ ppm) for cell assembly. Both cathodes and anodes were cut into discs with a diameter of 16 mm in the glovebox. A N/P ratio of 1.2 was used to prepare full cells. Anodes required for full cell investigations were prepared with the formulation of 93.0 wt % hard carbon (Kuranode Type II, 9 µm, Kuraray, Japan), 1.4 wt % C65 (Super C65, Imerys Graphite & Carbon, Switzerland), 1.87 wt % CMC (Sunrose MAC500LC, Nippon Paper Ltd. Japan), 3.73 wt % SBR (BM-4xx, Zeon Europe, Germany), as described in the work of Stüble et al.,[23] with a set areal loading of 1.37 mAh cm^{-2} ± 0.01 mAh cm^{-2}. A glass fiber separator (Whatman GF/C) and an electrolyte composed of 1 M $NaPF_6$ in EC and PC (w/w = 1:1) was used.

Material characterization.—X-ray diffraction (XRD): The powder sample was placed onto a Si wafer in an air-tight sample holder (Bruker, USA) inside an Ar-filled glovebox ($O_2 < 0.5$ ppm, $H_2O <$ 0.5 ppm). To ensure a flat surface, anhydrous DMC was added to the Si wafer and mixed with the sample. After DMC evaporation, the lid of the sample holder was closed and tightened. XRD was then performed on a Bruker D2 Bragg-Bretano diffractometer with Cu–Kα radiation. The reflection data were collected between 10° and 70° (2θ) at a scan speed of 0.02° s^{-1}.

TGA: TGA was conducted on a STA 449 F3 Jupiter (Netzsch Gerätebau, Germany) in an argon atmosphere. The temperature ranged from 25 °C to 1000 °C with a heating rate of 5 °C min^{-1}.

ICP-OES: Chemical composition was determined by means of an inductively coupled plasma optical emission spectrometer (iCAP 7600 Duo, Thermo Fisher Scientific, USA). For the measurements of the solid sample PW, it was dissolved first in 25 ml hydrochloric acid at 80 °C for 4 h in a graphite oven (EasyDigest, Analab, France).

Specific surface area measurement: Before measurement, each powder sample was placed into a glass vial, which was then connected to a sample degas system (VacPrep 061, Micromeritics Instrument Corporation, USA) for vacuum drying at 120 °C and

Table II. Summary of the different binders used in the cathodes. Abbreviations of binders are going to be used as reference for the electrodes which were prepared using said binder.

Abbreviation	Binder	Details
TRD	Fluorine acrylic hybrid latex	TRD202A, Eneos, Belgium
PAA	Polyacrylic acid	PAA ($M_v \sim 450$ k), Sigma Aldrich, United States
LA132	Ternary copolymer made of acrylamide, lithium methacrylate, and acrylonitrile	Viscosity ⩾4800 mPa·s (15 wt.-% aqueous dispersion, 40 °C), Xiamen TOB New Energy Technology, China
LA133	Ternary copolymer made of acrylamide, lithium methacrylate, and acrylonitrile	Viscosity 7300–9300 mPa·s (15 wt.-% aqueous dispersion, 40 °C), Xiamen TOB New Energy Technology, China
CMC	Carboxymethyl cellulose	Type 1: 2000 PA, IFF Speciality Products, Germany Type 2: Sunrose MAC500LC, Nippon Paper Ltd. Japan
PVDF	Polyvinylidene fluoride	Solef5130, Solvay, France

200 mTorr (0.27 hPa) for roughly 15 h. The specific surface area was measured by a surface area analyzer (Gemini VII2390a, Micromeritics Instrument Corporation, USA) and calculated based on Brunauer–Emmett–Teller (BET) theory.

Scanning electron microscopy (SEM): SEM micrographs were obtained by means of a Zeiss Supra 55 with an acceleration voltage of 3 kV. PW powder samples were adhered to a conductive tape and sputtered with a 2 nm gold layer onto the particles to improve the electric conductivity and reduce static charge of the sample.

Electrode characterization.—Resistivity Measurement: Bulk and interfacial resistance of the cathodes was determined using a multipoint measurement (RM2610 Electrode Resistance Measurement System, Hioki E.E. Corp., Japan). For each electrode at least five measurements were conducted, and the average value was reported.

Adhesion test: The adhesion strength of the electrode coating was measured using a 90 ° peel test conducted with a universal testing machine (Ametek LS 1). The coating was cut into three samples, each 30 mm wide, and adhered (coating side down) to a metal plate previously covered with double-sided adhesive tape. The samples were then rolled once with a 10-kg roller to ensure uniform contact. The adhesion force was measured using a 10-N load cell at a peel rate of 10 mm s^{-1}. The linear force (in N m^{-1}) was calculated based on the average adhesion force relative to the sample width.

Bending test: As the measurement of the adhesion test is performed in humid ambient conditions, an additional bending test was used to investigate the electrodes under dry conditions in an Ar-filled glovebox ($O_2 < 0.5$ ppm, $H_2O < 0.5$ ppm). The calendered electrode samples were transferred into the glovebox without further drying and cut into 1 cm in width and then bent around cylinders with diameters of 15 mm, 7 mm, and 3 mm to evaluate their mechanical flexibility and structural stability. After the test, the samples were visually inspected: if no visible cracks or defects appeared, the sample was rated as "Level 1"; if visible cracks were observed, it was rated as "Level 2"; and if delamination of the electrode coating from the substrate occurred, the sample was rated as "Level 3".

Electrochemical tests.—Galvanostatic tests: Cells were charged using a constant-charge-constant-voltage (CCCV) protocol and discharged under constant-current (CC) conditions between 2.0 and 4.0 V on BT2000 Battery Cycler (Arbin Instruments, USA) in a temperature-controlled chamber at 23 °C. After two formation cycles at C/20, the cells were tested at C/2 for 300 cycles with 2 cycles of C/20 employed after 50 cycles each to assess the degradation of the cathode active material. In the constant-voltage (CV) charging stage, the current was limited to C/50 for C/20 charging and to C/20 for C/2 charging. For each electrode, three cells were assembled, and the average capacity along with the corresponding standard deviation is reported in the results.

Electrochemical impedance spectroscopy (EIS): Impedance measurements were performed on full cells at the fully discharged state (2.0 V) on the MPG-200 Potentiostat (BioLogic, France) in a temperature-controlled chamber of 23 °C over a frequency range from 100 kHz to 10 mHz with an AC amplitude of 5 mV. One cell was used for each sample. After two formation cycles at C/20, the cells were cycled at C/2 for 100 cycles, followed by another 2 cycles of C/20 and 100 cycles at C/2. The impedance spectra were collected directly after formation, after 100 cycles at C/2 and after 200 cycles at C/2 and fitted by means of RelaxIS3 software.

Results and Discussion

Surface change and phase transitions of Prussian white during water-based processing.—As Prussian white is usually synthesized in an aqueous medium, water is naturally present in its crystal lattice, as pointed out by numerous studies.[12–15,18,19,24] Clavelin et al.[14] and Wang et al.[19] also reported the quick absorption of water by pre-dried PW after exposure to humid atmosphere. Therefore, it is essential to investigate the possible influences of water on PW during hydration and dehydration, which provides a firm grounding for further research in water-based electrode processing. Studies were performed with plain PW powder by mimicking comparable conditions as used in a typical water-based electrode processing route. Note that the coating and calendering steps were skipped due to their infeasibility with a powder sample.

First, the hydrated PW (H-PW) powder sample was dispersed in water without any pre-treatment step. In this case, moderate slurry drying conditions do not lead to a significant change of the particle morphology, see Fig. 1. The slight decrease in specific surface area from 1.75 m^2 g^{-1} to 1.36 m^2 g^{-1} is possibly due to partial dissolution of smaller PW particles and recrystallization on bigger particles. After the post-drying step, however, formation of cracks and an increase of the specific surface area by approximately a factor of four are observed.

If an additional pre-treatment step is applied, dehydrated PW (D-PW) is obtained with the specific surface area rising more than fourfold from 1.75 m^2 g^{-1} to 7.25 m^2 g^{-1} and initial cracks are already visible at the particle surface after this drying step, see Fig. 2. Despite moderate conditions, the subsequent drying of the dispersed particles now also leads to massive rise in the specific surface area, reaching approximately four times its previous value. At this stage, the particles have many cracks, and the surface structure changes significantly. These particles are so porous that the specific surface area does not grow further in the final post-drying step. It becomes clearly apparent that such repeated drying and hydration lead to cumulative structural damage of the PW. Please note that artefacts in the specific surface area measurement cannot be fully ruled out, since it requires vacuum drying for sample preparation that may induce additional influence. However, these artefacts are unlikely to alter the interpretation set out above. Its contribution to the measured specific surface area is expected to be small, because the vacuum

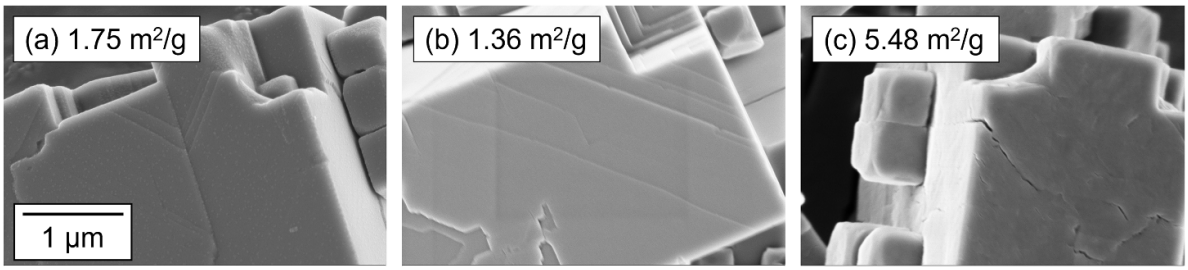

Figure 1. SEM micrographs with respective surface area of H-PW powder (a) as received, (b) slurry-dried, (c) post-dried.

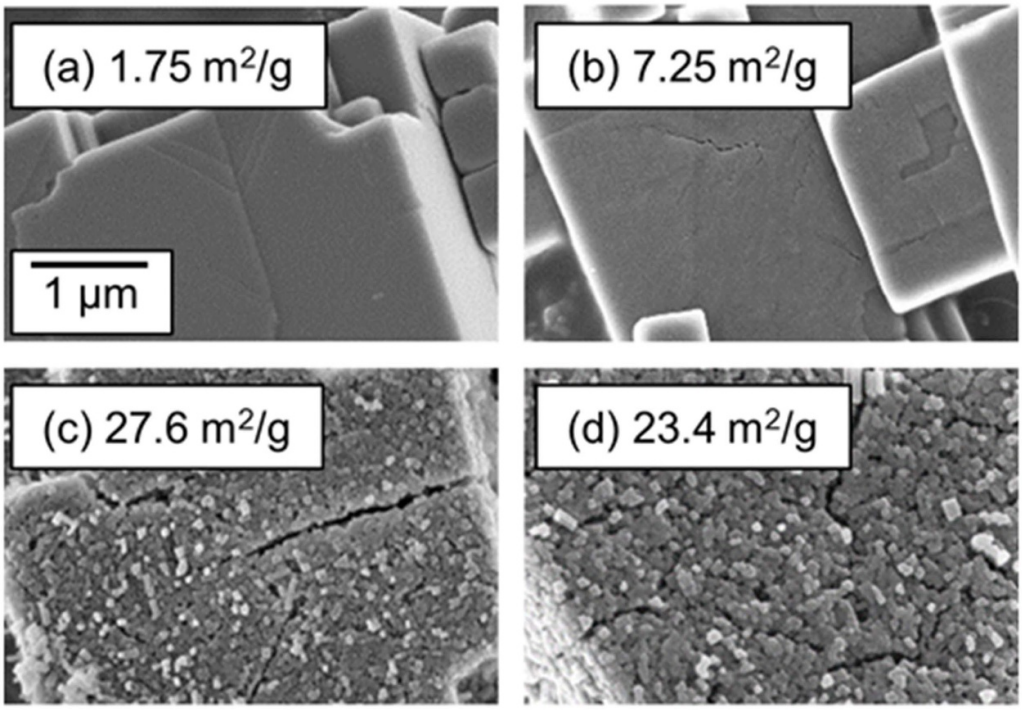

Figure 2. SEM micrographs with respective specific surface area of D-PW powder (a) as received (b) pre-treated (c) slurry-dried (d) post-dried.

level used for sample preparation was relatively low (0.27 hPa) compared with that applied during powder pre-treatment or post-drying ($< 10^{-3}$ hPa).

Since the as-received material contains 12.4 wt.-% of water (see Fig. A·1) originating from the aqueous synthesis route, the mechanical disintegration of the particles is mainly attributed to the stress induced by drying the particle to remove remaining crystal lattice water. These results are further supported by XRD analysis, which confirms that the uptake and release of water in the PW crystal lattice (see Figs. A·3 and A·4) during water-based processing is accompanied by phase transitions between monoclinic and rhombohedral and possible structural damage.[21,25]

With an additional pre-treatment step that induces subsequent phase transitions, a change in surface morphology becomes significantly visible. Therefore, the water in which both the D-PW and as received H-PW have been submerged for 6 h was filtered off and investigated via ICP-OES and pH-meter, see Table III. The PW-to-water mass ratio (58:100) was identical to that used in the actual slurry preparation. The remaining undissolved solid was also characterized via ICP-OES (see Table AI) and TGA (see Fig. A·5) and the resulting compositions are listed in Table III.

The D-PW powder shows more dissolution of transition metals as well as a higher pH value in comparison to H-PW. Both powders show a molar ratio of around 4: 1 of Na to Fe, which could indicate that the main material getting dissolved could be $Na_4Fe(CN)_6$. The dissolution of Mn is relatively small compared to the other two elements. The partial dissolution of $Na_4[Fe(CN)_6]$ can be expressed as:

$$Na_2Mn\left[Fe(CN)_6\right] \leftrightarrows Na_{2-4k}Mn\left[Fe(CN)_6\right]_{1-k} + kNa_4\left[Fe(CN)_6\right].$$

This could lead to additional vacancies in the PW lattice and create more defects, further increasing the surface area, while in parallel leading to the change in surface morphology observed in Fig. 2c. Next, the amount of dissolved material is higher for D-PW than for H-PW, which might suggest that the increased dissolution of $Na_4[Fe(CN)]_6$ is due to more PW surface being contacted by water. Here it should also be noted that the dissolution is not well reflected in the composition of the remaining solid presented in Table III. Independent of the pre-treatment, the composition of PW barely changes after contact with water at the investigated solid to liquid ratio because the dissolved substance accounts for only a very small portion of the pristine PW.

Impact of pre-treatment step on electrochemical properties.— To reveal the influence of the morphological changes of the PW particles, electrochemical characterization was performed with cells made from as-received PW (H-PW) and pre-treated PW (D-PW).

Table III. ICP-OES results of Na, Mn and Fe in water which submerged both H-PW and D-PW, pH values of the corresponding aqueous phase and composition of the undissolved solid phase determined by ICP-OES.

	Elemental concentration in ppm				
Sample	Na	Mn	Fe	pH	Composition of undissolved solid
D-PW	2740 ± 75	8.12 ± 0.24	1590 ± 38	9.3	$Na_{1.76}Mn[Fe(CN)_6]_{0.92} \cdot 2.5H_2O$
H-PW	483 ± 13	16.6 ± 0.5	301 ± 7	8.1	$Na_{1.77}Mn[Fe(CN)_6]_{0.93} \cdot 2.2H_2O$

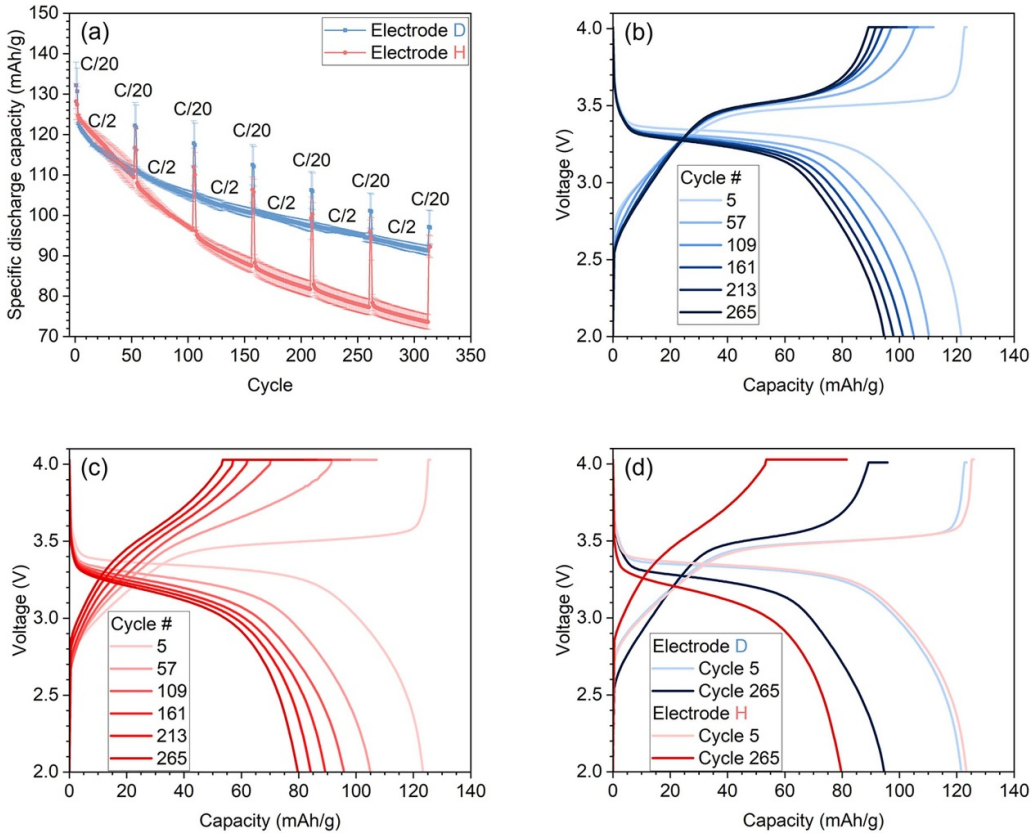

Figure 3. Electrochemical performance of electrode D and H in full cells: (a) long term cycling performance; (b) charge and discharge curves of electrode D at Cycle 5, 57, 109, 161, 213 and 265; (c) charge and discharge curves of electrode H at Cycle 5, 57, 109, 161, 213 and 265; (d) comparison between electrode H and electrode D in terms of charge and discharge at C/2 at Cycle 5 and Cycle 265, respectively. Note: The data from one representative cell of each electrode were selected for the charge and discharge curves presented in (b)–(d).

Electrodes prepared from H-PW and D-PW are denoted as electrode H and electrode D, respectively, while the corresponding full cells assembled after post-drying are referred to as cell H and cell D. The labels H and D refer exclusively to the state of the PW powder before slurry preparation and do not indicate the hydration state of PW after slurry mixing, coating, or drying. As presented in Fig. A·6, both electrode D and electrode H obtained after coating and slurry drying contain hydrated PW (monoclinic phase). Following a proper post-drying step in a vacuum furnace, PW in both electrodes transforms into the dehydrated rhombohedral phase, thereby reducing the risk of parasitic reactions induced by the residue water in the full cells. The electrodes were manufactured via the aqueous processing route using a binder blend of 2.0 wt.-% CMC + 4.0 wt.-% of TRD. Drying conditions are specified as in Table I. Figure 3 represents the electrochemical performance of the electrodes fabricated using either as-received or pre-treated PW.

Figure 3a presents the galvanostatic performance of electrode D and electrode H. Both electrodes deliver a comparable high initial specific discharge capacity at 0.05 C, namely 128 ± 4 mAh g^{-1} for electrode H and 132 ± 6 mAh g^{-1} for electrode D, corresponding to roughly 80% of the theoretical capacity. This initial capacity loss is likely associated with SEI formation on the anode side. During the first 40 charge–discharge cycles at 0.5 C, electrode H made from as-received AM exhibits a slightly higher specific discharge capacity, which is in good agreement with its lower bulk resistivity and interfacial resistance (see Fig. A·7). A possible explanation for the slightly lower capacity of electrode D during the first 40 cycles is the higher dissolution of D-PW in H_2O in the form of $Na_4[Fe(CN)]_6$, as displayed in Table III. This possibly promotes mechanical destabilization associated with newly created surface and impairs electrochemical performance, as the theoretical capacity of $Na_4[Fe(CN)]_6$ is significantly lower (88.2 mAh g^{-1}) and it shows poor electronic conductivity, which could hinder electron transport if it accumulates at the surface of the material.[26,27] Another factor to be taken into account is the slurry pH (see Table AII). The slurry prepared from D-PW (pH = 9.9) is more basic than that prepared from H-PW (pH = 7.9). The higher pH may promote corrosion of the aluminum current collector and thereby contribute to the

overall impedance of the resulting electrode. These resistive effects are expected to be less significant at a low current density, such as C/20.

As cycling proceeds further, electrode H shows a substantially faster capacity fade at 0.5 C compared to electrode D, which was produced with pre-dried PW, while the capacity difference at 0.05 C remains nearly constant. The difference in capacity retention at 0.5 C may be attributed to variations in the particle surface characteristics. As observed in the dispersion experiments mentioned above, multiple phase transformations take place during water-based electrode fabrication. The active material particles in electrode D experience three phase transitions (namely: monoclinic → rhombohedral → monoclinic → rhombohedral, see Fig. A·3) during processing, which leads to more pronounced cracking and an approximately fourfold increase in specific surface area. This cracking due to electrode fabrication is less significant in electrode H, in which PW only undergoes one phase transition, i.e. monoclinic → rhombohedral (see Fig. A·4). The presence of cracks prior to galvanostatic cycling could be beneficial by providing internal buffering space, which has been observed for other porous battery materials such as nickel-manganese-cobalt layered oxides[28] or silicon.[29] This is particularly important for Mn-containing PW, which undergoes significant volume changes during oxidation and reduction due to Jahn Teller effect.[30–32] Post-mortem SEM analysis (see Fig. A·8) supports this hypothesis. While electrode D with pre-treated PW shows no noticeable change in particle surface morphology after cycling, electrode H exhibits a higher density of pores and cracks formed during galvanostatic cycling after more than 300 cycles. The formation of new cracks during cycling is associated with the phase transitions during charge and discharge between rhombohedral and tetragonal phases,[11,18] which could cause the degradation of the AM upon cycling. Electrode D contains many short cracks on the particle surface before cycling and most of them have a length of less than 0.5 μm (see Fig. A·8a). In comparison, fewer but longer cracks (in the order of magnitude of 1–2 μm) are observed in electrode H before cycling (see Fig. A·8c). The difference in size may result in the difference in crack propagation according to Griffith's crack theory. The critical flaw size is, however, difficult to calculate due to unavailable mechanical properties of PW such as the fracture toughness or Young's modulus.

The cracking behavior is also reflected in the charge–discharge profiles. Figures 3b and 3c exhibit the development of charge and discharge curves of electrode D and electrode H in a full cell, respectively. At early cycles such as the 5th cycle, no significant difference between two cells is visible, in spite of a slightly lower overpotential and higher specific capacity of cell H. As cycling proceeds, cracking takes place so that the overpotential of both cells increase, but the increase is more pronounced for electrode H. To compare the evolution of overpotentials of both cells, the charge and discharge curves of both cells in Cycle 5 and 265 are plotted together in one graph (Fig. 3d). Whereas electrode D maintains a relatively flat plateau even after 265 cycles, the plateau of charging and discharging of cell H becomes significantly more sloped at the 265th cycle compared to that at the 5th cycle. The higher overpotential in cell H than cell D is also reflected by a markedly longer CV step of cell H.

To investigate the influence of cracking on electrode impedance, EIS measurements were performed. Figures. A9 and A10 display the results of impedance measurements on full cells in Nyquist and Bode plots, respectively, at fully discharged state (2.0 V). It should be noted that initial sample refers to the cell undergoing two formation cycles prior to the long cycling stability tests.

To determine the most appropriate equivalent circuit model, distribution of relaxation time (DRT) analysis was performed on the EIS data and presented in Figs. A·11a and A·11b. Since cell D and cell H differ only in the positive electrode (PW), a comparison between the impedance of the full cells could provide some information about the change of PW. Nevertheless, because the measurements were performed on full cells, the individual contributions of the positive and negative electrodes cannot be completely separated.

For cell D with positive electrode D and hard carbon negative electrode, a small peak at the high frequency range (>1000 Hz) is observed and associated with the formation of surface film.[33–35] Directly after formation cycles at C/20, this cell exhibits a shoulder between 3 and 100 Hz (corresponding to charge transfer[34]) and a broad peak related to diffusion behavior at a lower frequency range. After cycling at C/2 for 100 or 200 cycles, a separate broader peak is observed at the medium-low frequency range between 0.2 and 100 Hz is observed instead of just one shoulder, together with a peak ascribed to diffusion below 0.1 Hz.[35] For cell H, a small peak at the medium-high frequency range (>300 Hz) linked with formation of the surface film is observed and diffusion behavior corresponds to the peak at the low frequency range (<1 Hz). Similar to cell D, the cell H shows a shoulder between 3 and 100 Hz, while a peak between 1 and 100 Hz after the cell is cycled for 100 or 200 cycles at C/2. It is also noteworthy that the low-frequency region below approximately 1 Hz does not exhibit the typical 45° line expected for ideal semi-infinite diffusion in the Nyquist plots. Instead, the spectra progressively approach a more horizontal response with decreasing frequency, particularly after 100 and 200 cycles. Consistently, the magnitude of the low-frequency phase angle in the Bode plots decreases from approximately 30° to approximately 10° after long-term cycling. The reason could be an overlap of different diffusional processes such as the diffusion in the porous electrode, the diffusion in separator as well as the diffusion in the active part, as discussed by Talian et al.[35] A reliable representative equivalent circuit to simulate this process is difficult to find and hence the low-frequency region is excluded to achieve better fitting (<1 Hz for both cells). To simplify the contribution of diffusion to the impedance at medium and high frequency range between 1 Hz and 100 kHz, a standard Warburg element is still used. To summarize, an equivalent circuit is selected consisting of one resistor for bulk resistance of the battery such as electrode and electrolyte, two circuits with a resistor and a constant phase element in parallel (R/CPE) for surface film and charge transfer, respectively, and a Warburg element for the diffusion (see Fig. A·11c). The CPE exponent α is fixed after the first fitting step for each cell to reduce the fitting error of CPE parameter Q. The resulting fitting parameters are listed in Table AIII.

As is illustrated by Nyquist plots in Fig. A·9, cell H has a smaller Ohmic resistance (3.7 Ω) than cell D (9.3 Ω), which agrees quite well with the resistivity measurement presented in Fig. A·7. The mild decrease of Ohmic resistance in both cells with charge and discharge could be due to improved electrolyte wetting or internal contact. The small depressed semicircle at high frequency range provides the information of surface change in both electrodes in the two cells. Cell D has a surface film resistance R_{SF} of 2.0 Ω before long-term cycling and this value decreases after 100 cycles (1.7 Ω). Cell H shows a similar trend with R_{SF} of 1.5 Ω initially and of 1.2 Ω after 100 cycles at C/2. This may be related to surface film formation and stabilization at early stages of cycling. When the two cells are further cycled at C/2, an increase of 29% in the resistance of surface film in cell D, while the R_{SF} of cell H nearly triples. This is consistent with the post-mortem SEM analysis exhibited in Fig. A·8. As cycling proceeds, repeated volume changes in the positive electrode may promote crack formation and propagation and expose fresh particle surfaces. This takes place more mildly in cell D probably due to the influence of pre-exisiting small cracks as discussed above. The second depressed semicircle, which is located in the medium frequency region, exhibits the reaction kinetics. Cell D has a low initial R_{ct} of 14.7 Ω, which can be associated with the high porosity of PW particles in electrode D shown in Fig. A·8a. The resistance of charge transfer grows drastically as cycling proceeds (94 Ω after 100 cycles at C/2 and 123 Ω after 200 cycles at C/2), indicating progressively slower reaction kinetics after charge and discharge. In comparison, cell H possesses a high initial R_{ct} of 162 Ω owing to much less initial surface area. It drops moderately with cycling to 127 Ω after 100 cycles and remains relatively stable between 100 and 200 cycles at C/2 (132 Ω). This trend is in good agreement with the

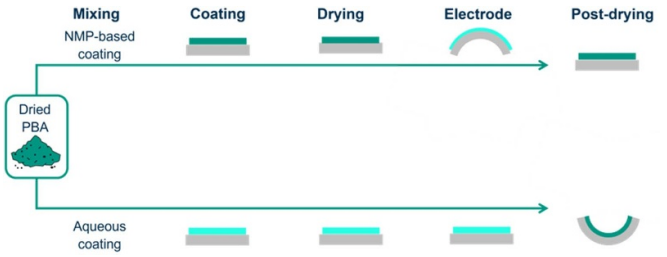

Figure 4. Warping directions of PW electrode of NMP-processed and water-processed electrodes. Gray represents the aluminum substrate. Dark green indicates PW is rhombohedral, while light green indicates PW is monoclinic.

crack formation observed Fig. A·8d, as the newly generated surfaces may temporarily increase the electrochemically accessible area and thereby facilitate charge transfer. Overall, cell H has a higher R_{ct} than cell D over the investigated cycling period, accounting for its higher polarization and faster capacity decay at C/2 observed in Fig. 3a. It should again be emphasized that the impedance measurements were performed at the full-cell level. The interpretation therefore assumes that the other cell components, including the electrolyte and the hard-carbon negative electrode, undergo comparable changes in both cells, such that the observed impedance differences arise predominantly from the positive electrodes.

In summary, cracks introduced during slurry mixing of PW before cycling may contribute to a longer cycle life by accommodating cycling-induced strain. On the other hand, the higher specific surface can also increase the dissolution and result in higher ohmic resistance and possible deterioration of reaction kinetics.

Electrode manufacturing using pre-treated PW powder.—The previous study has shown that pre-drying step has a beneficial effect on the service life of aqueous-processed Prussian white full cells. The results are compared with NMP-based electrode samples using the same mass loading and processing conditions below.

Electrode bending: A significant difference, depending on the medium used for electrode manufacturing, can be seen in Fig. 4 for the warping behavior of the electrodes at various processing steps. When pre-dried PW is processed in a conventional way with PVDF in NMP into an electrode, the freshly coated and dried electrode starts absorbing moisture from the atmosphere due to the hygroscopic nature of PW. The water absorption into the crystal lattice leads to a phase transition from rhombohedral to monoclinic, during which the crystal expands by + 23%, calculated on the basis of the experimental crystallographic data reported by Song et al.[11] The PW particles at the bottom layer are firmly adhered to the aluminum foil via the binder, thereby limiting their deformation. This accounts for outward warping (arched away from the current collector) of the NMP-processed electrode. The curvature can be flattened by subsequent post-drying step, where a volume contraction takes place due to phase transition from monoclinic to rhombohedral.

In contrast, in the aqueously processed electrode, the PW exists mainly in its monoclinic (hydrated) form because of exposure to water during dispersion in water. After drying at room temperature directly following coating, the interstitial water remains in the structure. During post-drying step at 130 °C under vacuum, this type of water starts to diffuse out of the crystal, resulting in a volume shrinkage.[12,18,21] This explains the inward warping (arched toward the current collector) of water-processed electrodes.

While inward warping of water-processed PW electrodes upon post-drying is induced by water removal, this effect is not universal for water-processed electrodes and depends on the active material. For comparison, an LFP electrode with comparable mass loading prepared from a water-based formulation remained flat before and after post-drying (see Fig. A·12. The distinctive behavior of PW, however, arises from its intrinsic changes of the crystal structure. Compared to LFP, which theoretically has no crystal water (for TGA results, see Fig. A·1), Prussian white contains a large amount of water inside the crystal.[14,18,24,36] This indicates that active material also contributes to electrode warping upon post-drying. At proper drying conditions (130 °C, 15 h, 10^{-3} bar) as used in this study, the interstitial water can be removed, during which a volume shrinkage of approximately 19% due to phase transition from monoclinic (hydrated) to rhombohedral (dehydrated) takes place.[7] The phase transition and the correlated decrease in volume stress the coating and lead to warping of the overall electrode.

Resistivity: Apart from warping directions, a clear difference lies in bulk resistivity and interfacial resistance (see Figs. 5a and 5b). Electrodes obtained by NMP-based processing have a lower bulk resistivity (4.3 ± 0.2 Ω·cm) before post-drying than those by water-based processing (12.2 ± 0.3 Ω·cm). In contrast, the interfacial resistance shows the opposite trend with 2.8 ± 0.4 Ω·cm^2 for the NMP-based electrode and 0.38 ± 0.03 Ω·cm^2 for the water-based. The lower bulk resistivity of the NMP-processed electrode can be explained by the solubility of both binders (PVDF and PAA) in the processing medium, favoring their interaction with conductive additives to form a conductive network. The hydrophobic binder PVDF has more affinity to conductive additives, favoring the formation of conductive carbon binder domains, as observed by Weber et al.,[37] who investigated the surface free energy of different components in electrodes. In contrast, the water-based latex binder TRD is insoluble and thus less effective in forming the carbon binder domains. The relatively high interface resistance of the NMP-based electrode is likely to be attributed to the insufficient contact between electrode layer and aluminum foil, as NMP-based electrode shows a lower adhesion strength (see Fig. 5c, 5.3 ± 2.1 N·m^{-1}) than the water-based counterpart (9.3 ± 1.2 N·m^{-1}). Another factor contributing to the higher bulk resistivity and interfacial resistance of the water-processed electrode is the dissolved substances from PW into water, for example, $Na_4Fe(CN)_6$ as discussed above as well as possible hydroxide as suggested by Ojwang et al.[7]

The comparison of NMP-and water-based systems, as well as the influence of post-drying are shown in Figs. 5a and 5b. A growth in both types of resistivity is observed in both electrodes: while the NMP-processed electrode delivers a bulk resistivity of 18.9 ± 1.2 Ω·cm and an interfacial resistance of 6.6 ± 1.4 Ω·cm^2 after post-drying, the aqueously processed electrode shows 14.1 ± 1.5 Ω·cm and 0.72 ± 0.13 Ω·cm^2, respectively. The increase is attributed to shrinkage of polymeric binders due to further solvent removal. The shrinkage might cause local loss of contact between different components of the electrode and result in a rise in resistance. However, a larger increase is observed in the NMP-processed electrode, particularly in interfacial resistance, despite the same conditions for post-drying. A possible explanation is the possible creep behavior of PVDF at the high temperature during post-drying (130 °C), as suggested by Huttner et al. during their investigation in post-drying of nickel-cobalt-manganese-oxide electrode with PVDF at 120 °C.[38] They claim that the creeping of PVDF might cause rearrangement of the carbon black particles, therefore damaging the integrity of carbon-binder domains. Another possible explanation is that the elevated temperature accelerates the defluorination and crosslinking of PVDF molecules. PW, especially dehydrated PW, shows a higher basicity (see Table III), which might catalyze the crosslinking of PVDF according to the reaction mechanism mentioned by Roberts et al.[22] Consistent with this, in our first attempt to fabricate slurry with only PVDF, gelation occurred immediately after stirring stopped. PAA was therefore added in a subsequent trial to partially mitigate the basic condition, extending the coating window to approximately 30 min before gelation occurs within the slurry residue. The temperature increase during post-drying may enable further crosslinking of PVDF. The elimination of the fluoro group during crosslinking weakens the adhesion of electrode on the aluminum foil, since the dipole-dipole interaction between F atoms in the chain backbone and H atoms on the surface of the

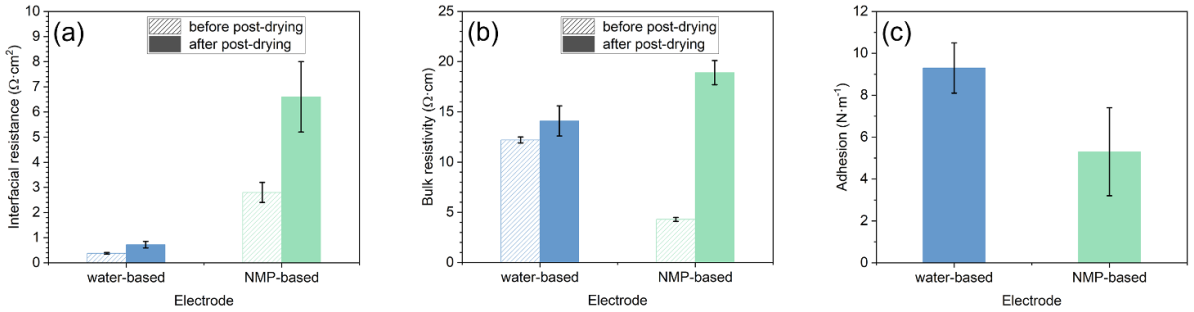

Figure 5. (a) Interfacial resistance and (b) bulk resistivity of NMP-and water-processed electrodes before and after post-drying, (c) adhesion of NMP-and water-processed electrodes before post-drying. Adhesion of both electrodes after post-drying was not measured due to difficulty of sample preparation without creating cracks.

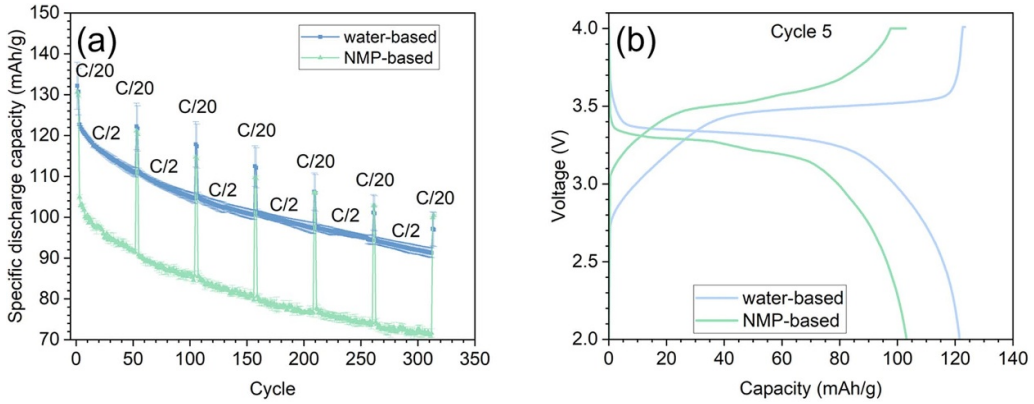

Figure 6. Electrochemical performance of NMP and water-based PW electrodes in full cells: (a) long-term cycling, (b) charge and discharge curve at the 5th cycle (C/2). Note: The data from one representative cell of each electrode were selected for the charge and discharge curves presented in (b).

current collector or active material is crucial to the bonding effect of PVDF.[39] At the same time, PW loses surface-adsorbed water during post-drying, lessening the interaction between PW and PVDF, as hydrogen associated with surface-adsorbed water on the active material is no longer available. Therefore, both bulk resistivity and interfacial resistance rise after post-drying.

Electrochemical performance: To further evaluate the change in electric resistivity, coin cells were built with NMP-processed electrodes after post-drying for electrochemical characterization and compared to water-processed electrodes. Figure 6a shows the long-term cyclability of NMP-processed and water-processed PW electrodes at C/2. Whereas no significant difference in specific discharge capacity at C/20 can be observed (130.7 $\pm$ 0.6 mAh g^{-1} for NMP-based and 132 $\pm$ 6 mAh g^{-1} for water-based in the first cycle), a difference of roughly 20 mAh g^{-1} is visible when the C-rates increases from C/20 to C/2 (104.9 $\pm$ 0.6 mAh g^{-1} for NMP-based vs. 122.7 $\pm$ 0.2 mAh g^{-1} for water-based in the third cycle), indicating higher resistance of the NMP-processed electrode than the water-processed counterpart. On the charge and discharge curve (Fig. 6b), a bigger overpotential can be detected between the charge and discharge plateaus, especially at the beginning of charge or discharge, when a difference of 0.2–0.3 V in voltage is observed between the NMP-and water-based electrode. This agrees well with the resistivity results presented in Fig. 5, since a higher bulk resistivity and interfacial resistance in the electrode produced in NMP adds to a larger overpotential. In addition, PVDF degradation may contribute to the impedance increase, as suggested by Goswami et al. They reported that PVDF degradation could occur during electrode fabrication and continue after electrolyte wetting and cycling, accompanied by the formation of an unstable and resistive cathode–electrolyte interphase.[40]

It is also evident from Fig. 6a that at a low C-rate such as C/20, the NMP-processed electrode shows a lower degree of degradation. The average specific discharge capacity of the NMP-processed electrodes is 100.4 $\pm$ 0.2 mAh g^{-1} while that of the water-processed electrodes is 97 $\pm$ 4 mAh g^{-1}. This suggests that the reduced capacity of NMP-processed electrode at C/2 is not primarily because of material degradation but rather dominated by polarization effects. The slightly lower capacity of the water-processed electrodes at the 314th cycle is possibly related to dissolution of transition metals (Mn and Fe) induced by contact with water as presented in Table III. The dissolved transition metal ions remain in the electrode after processing and can migrate to the anode side, as has been reported by Büchele et al. in their investigations on PW/hard carbon full cells.[20] This migration results in a loss of redox-active centers and reduction in specific capacity.

Challenge of substituting PVDF with water-based binders.— The results presented above have demonstrated the possible adverse influence of drying history and exposure to water on the AM particle integrity, which can further influence the mechanical stability of the resulting electrodes. This emphasizes the significance of proper binder selection in the water-based production of PW electrode, as the binder system has a strong influence on electrode integrity. As next step, various combinations of CMC and a second binder such as TRD, PAA, LA132, and LA133 are investigated in order to possibly reduce the amount of fluorinated binder. Adhesion and resistance measurements were carried out for the resulting electrodes, see Figs. 7a–7c. While all freshly prepared PW electrodes momentarily exhibited flat surfaces without curvature (see Fig. A·12), the electrode using PAA as a secondary binder developed many cracks during coating and drying. As a result, it was not possible to prepare a

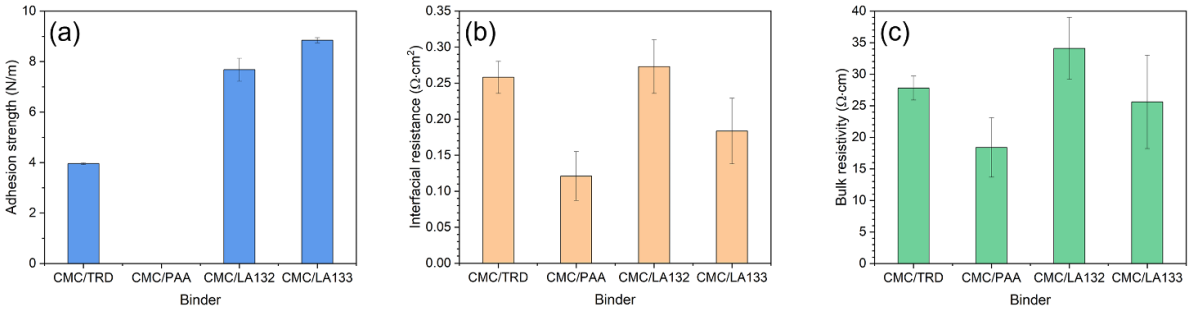

Figure 7. (a) Adhesion strength, (b) interfacial resistance and (c) bulk resistivity of electrodes with different water-based binder combinations using CMC and either TRD, PAA, LA132 or LA133 as a second binder. The adhesion strength of PAA blended electrodes was not measurable due to crack formation and therefore excluded.

defect-free sample for adhesion test. This behavior is possibly related to the strong water-uptake capacity of PAA (see Table AIV). Upon drying at room temperature directly after coating, water can be partially removed from the swollen macromolecular network, causing the network to shrink.[41,42] Therefore, this sample was excluded from adhesion test, while resistance measurement was performed in a defect-free zone of the coating, not affected by partially occurring delamination and crack formation that made the sample CMC/PAA unsuitable for adhesion strength measurement and further electrode processing.

Adhesion: Measurable electrodes show an adhesion strength of 4.0 ± 0.1 N·m^{-1} for TRD-based electrodes, 7.7 ± 0.5 N·m^{-1} for LA132-based and 8.8 ± 0.1 N·m^{-1} for LA133-based, ranked from lowest to highest, and are all mechanically stable enough for further investigations. The adhesion strength increases by using LA132 and LA133. A plausible reason is the difference in the structure and polarity of the latex binders. When comparing the different binders, TRD is a fluorinated acrylic hybrid latex containing ester groups, whereas the LA binders contain not only carboxylate but also amide and nitrile groups. These additional polar functional groups are therefore regarded to be responsible for the enhanced particle-substrate adhesion observed in the two LA-based electrodes.[37,43–47] This difference in polarity is also reflected in their ability to absorb water when exposed to humidity (dew point 25 °C), see Table AIV: the TRD-based carbon-binder coating exhibits a water content of $15 \cdot 10^3$ ppm, while LA132-based and LA133-based coating can absorb $20 \cdot 10^3$ ppm and $22 \cdot 10^3$ ppm of water, respectively.

Resistivity: When comparing this to the interfacial resistance and bulk resistivity of the electrodes, there are multiple differences between the various binder systems. For the interfacial resistance, electrodes prepared with TRD and LA132 show comparable results with 0.26 ± 0.02 Ω cm^2 and 0.27 ± 0.04 Ω cm^2, respectively. In comparison, the electrode using LA133 exhibits a lower interfacial resistance with 0.18 ± 0.05 Ω cm^2, while the electrode containing PAA delivers the lowest value at 0.12 ± 0.03 Ω cm^2. When observing the bulk resistivity, electrodes using LA132 show the highest result with 34 ± 5 Ω cm, which drops to 28 ± 2 Ω cm for TRD and 26 ± 7 Ω cm for LA133, followed by PAA with 18 ± 5 Ω cm. The TRD-based electrode shows bulk resistivity and interfacial resistance between those of LA132-and LA133-based electrodes, owing to its different intrinsic electrical resistance. In the case of PAA, its solubility plays a key role. The binder molecules are more homogeneously distributed in the electrode composite and therefore more likely to be adsorbed on CB, compared to insoluble latex particles such as TRD. This helps disperse and stabilize the conductive additives and contributes to the formation of carbon-binder domains. The acidity of PAA could also play a role in removing hydroxides present on the particle surface[7] and hence lower the contribution of these species to the overall resistance. In contrast, the other three co-binders exist as suspension in water and contribute barely to the dispersion of conductive additives. This explains the higher bulk resistivity.

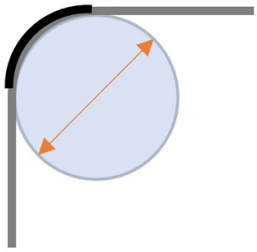

Figure 8. Schematic of bending test over a 90 ° angle. The diameter indicated by the orange arrow varied from 3 mm to 15 mm.

Bending test: The results described above underline that post-drying causes a pronounced change in the mechanical properties of PW electrodes. Therefore, it is reasonable to further evaluate the mechanical behavior of the electrodes after post-drying at 130 °C for 15 h under vacuum by using the bending test. A schematic of the bending test and the subsequent results are summarized in Fig. 8 and Table IV.

All tested electrodes before post-drying withstand bending around cylinders of 15 mm and 7 mm in diameter. As the diameter decreases to 3 mm, TRD-based electrodes delaminate, whereas electrodes with LA-based binders survive bending with only a limited number of cracks. This observation is consistent with the adhesion test results, confirming a correlation between the two mechanical evaluations. In comparison, the results for the mechanical stability provided by the bending test change after post-drying for LA132 and LA133. The mechanical integrity for both binders decreases and electrodes show defects, whereas TRD-based electrodes show the same properties, which can be associated with their ability to retain water presented in Table IV. This leads to the proposal that PW-based electrodes under ambient conditions regarding their mechanical strength are not representable to the PW electrodes used in the battery, as the mechanical integrity is drastically impacted by the post-drying.

Electrochemical performance: In addition to mechanical tests, electrochemical analyses were also carried out on electrodes containing TRD, LA132 and LA133, respectively, in full cells with hard carbon. As noted above, the latter two electrodes developed cracks after post-drying and artefacts arising from electrode damage cannot be fully excluded in spite of careful handling during cell assembly. Considering the possible disadvantages associated with the lower content of conductive additives, the discharge cutoff voltage was lowered to 1.5 V so that the cells could complete discharge. The results of galvanostatic cycling are illustrated in Fig. A·13. As exhibited in Fig. A·13a, all three electrodes show similar initial specific discharge capacities: 136.2 ± 0.4 mAh g^{-1} for the TRD-based, 135.5 ± 0.6 mAh g^{-1} for the LA132-based and 135 ± 1 mAh g^{-1} for the LA133-based in the first cycle. As soon as the C-rate increases from C/20 to C/2, the behavior of the electrodes with LA132 and

Table IV. Comparison of flexibility of electrodes with combinations of CMC and different binders before and after post-drying (Level 1: no visible cracks or defects appear. Level 2; cracks are observed. Level 3: delamination of the electrode occurs).

	Before post-drying			After post-drying		
Second binder	15 mm	7 mm	3 mm	15 mm	7 mm	3 mm
TRD	1	1	3	1	1	3
LA132	1	1	2	2	2	3
LA133	1	1	2	2	2	3

Table V. Summary of the mechanical, electrical, and electrochemical performance of electrodes prepared with different conditions.

(a) *Pre-treeatment*

Pre-treatment	Electrical resistivity	Initial discharge capacity (C/20)	Cycling stability (C/2)
Yes	+	+ + +	+ +
No	+ + +	+ + +	+

(b) *NMP vs water*

Dispersing medium	Adhesion before PD	Electrical resistivity after PD	Initial discharge capacity (C/20)	Cycling stability (C/2)
NMP	+ +	+	+ + +	+
Water	+ + +	+ +	+ + +	+ +

(c) *Different aqueous binders*

Binder combinations	Adhesion before PD	Flexibility after PD	Electrical resistivity	Initial discharge capacity (C/20)	Cycling stability (C/2)
CMC/TRD	+ +	+ +	+ +	+ + +	+ +
CMC/PAA	+	n.m.	+ + +	n.m.	n.m.
CMC/LA132	+ + +	+	+	+ + +	+
CMC/LA133	+ + +	+	+ +	+ + +	+

LA133 changes drastically and both witness a significant capacity loss within the first 10 cycles after the increase of the C-rate, amounting to 21.4% and 23.8%, respectively. In contrast, the TRD-based electrode still delivers a specific discharge capacity of more than 123 mAh g^{-1} during the first 10 cycles at C/2 before a more pronounced capacity decline takes place in the later cycles. After being cycled at C/2 for 50 cycles, the TRD-based electrode also shows capacity fading, retaining only 66% of its initial capacity at C/2 (127.7 $\pm$ 0.1 mAh g^{-1} in Cycle 3). In the 53rd cycle, the C/20-checkup cycle after C/2 cycling, the electrode containing TRD still gives a specific discharge capacity of 123.0 $\pm$ 0.9 mAh g^{-1}, whereas the cells with LA132-and LA133-based electrodes reach only 89 $\pm$ 4 mAh g^{-1} and 85 $\pm$ 3 mAh g^{-1}, indicating that LA-based electrodes might have undergone more severe irreversible Na inventory loss, while this effect appears to be much less pronounced for TRD-based electrode.

A closer inspection of the charge–discharge curves in the first few cycles provides further insight into the different electrochemical behaviors of the TRD-and LA-binder-based electrodes (Figs. A·13b–A·13d). Compared with the TRD-based electrode, the electrodes containing LA-binders not only show a higher overpotential, but also an additional plateau at roughly 3.45 V, which may be associated with formation of an intermediate phase. This plateau disappears from Cycle 7 onward for both LA-binder-based electrodes, accompanied by a dramatic loss of specific discharge capacity. No such plateau is observed in the electrode with TRD, pointing to a possible contribution of LA132 and LA133 to side reactions. As discussed above, both LA132 and LA133 possess additional functional groups such as amide and nitrile and are capable of retaining water after post-drying. These characteristics may promote side reactions in the first few cycles and therefore account for the faster capacity decay of the electrodes with LA132 or LA133 in the early cycles than the TRD-based electrode. The capacity decay of TRD-based electrodes has been discussed in a previous chapter (see *Impact of pre-treatment step on electrochemical properties*) with respect to Electrode H. Since the TRD-based electrode used here contains even lower amount of conductive additives, it is even more susceptible to overpotential due to its higher resistance.

To summarize, despite good mechanical stability provided by LA-binders directly after electrode processing, they cannot maintain sufficient adhesion and cohesion after post-drying and lead to side reactions during charge and discharge. Therefore, the initial choice of TRD-binder proves to be superior to LA-binders. For further optimization of the formulation, not only the mechanical properties during electrode coating and drying and calendering but also the stability after post drying and the resulting electrochemical performance must be kept in mind.

Conclusions

In this work, we have demonstrated several challenges of fabricating PW electrodes in an aqueous medium and studied the selection of binders and pre-treatment of the AM and their impact on the resulting electrodes. A qualitative comparison of the effects of PW pre-treatment, dispersing medium, and aqueous binder selection on the mechanical, electrical, and electrochemical properties of the resulting electrodes is provided in Table V. Firstly, as-prepared Prussian white (PW) contains approximately 12 wt.-% water in the crystal structure and the removal of water induces phase transformation and volume shrinkage. Pre-treatment of PW and subsequent water-based processing leads to substantial surface change and crack formation as repeated vacuum drying and exposure to water trigger back-and-forth phase transformations when crystal water is incorporated and removed from the lattice. At the same time, direct contact with water promotes partial dissolution of lattice ions, primarily Na^+ and $[Fe(CN)_6]^{4-}$, generating vacancies within the crystal structure.

Secondly, when pre-treatment of PW by vacuum drying is omitted and the as-received material is directly used for slurry preparation, the change of the surface particle is less pronounced; however, the resulting electrodes after post-drying exhibit faster degradation and a shorter cycle life, likely because the more compact and less porous particle morphology provides only limited buffering effect. Thirdly, although conventional NMP-based processing results in flat electrodes after post-drying, the resulting electrodes exhibit high bulk resistivity and interfacial resistances. This leads to increased overpotentials and limits its application for cycling at higher C rates. In contrast, despite inward warping of water-processed electrodes after post-drying and possible concerns about its mechanical integrity, the electrode delivers superior specific discharge capacity over the NMP-processed counterparts. Last but not least, while water-based processing offers advantages in the electrochemical performance of the resulting electrodes, switching from NMP-based to water-based processing requires proper binder selection to ensure sufficient mechanical stability of PW electrodes after post-drying. Among the four investigated binder combinations, CMC/TRD provides the best balance in terms of electrode flexibility, structural integrity as well as electrochemical performance. Overall, these findings highlight a trade-off between maintaining mechanical stability of AM particles as well as electrodes and achieving long-term electrochemical cyclability in water-processed PW electrodes.

Acknowledgment

This work contributes to the research carried out at CELEST (Center for Electrochemical Energy Storage Ulm Karlsruhe) and Material Research Center for Energy Systems (MZE). It was funded by the Deutsche Forschungsgemeinschaft (DFG, German Research Foundation) under Germany's Excellence Strategy—EXC 2154—Project Number 390874152 (POLiS Cluster of Excellence).

Large language models were used during the drafting of this article for improvement of readability. All data analysis, interpretations, conclusions and final revisions were conducted by the authors, who take the full responsibility for the accuracy, validity and originality of the content presented.

The authors would like to acknowledge Sebastian Büchele (Litona GmbH) for developing the synthesis route for Prussian white, Dr Valeriu Mereacre (IAM) for synthesizing the cathode active material and Dr Andreas Hofmann (IAM) for supplying the electrolyte. Special thanks are extended to Dr Thomas Bergfeldt (IAM) for elemental analysis via ICP-OES. The authors also thank Christina Odemer (IAM) for performing TGA, Monika Raab (IAM) for BET-measurements and Ruochen Xu (IAM) and Hanqing Sun (IAM) for their valuable comments and suggestions on the manuscript.

Appendix

Table A·I. ICP-OES results of as-received PW and PW washed with water (undissolved part).

	Mass percentage (wt.-%)			Molar ratio to Mn		
Sample	Na	Mn	Fe	Na	Mn	Fe
as-received	11.8 ± 0.3	16.1 ± 0.5	15.0 ± 0.3	1.75	1	0.92
H-PW washed with water	13.5 ± 0.4	18.2 ± 0.5	17.2 ± 0.4	1.77	1	0.93
D-PW washed with water	13.4 ± 0.4	18.2 ± 0.5	17.0 ± 0.4	1.76	1	0.92

Table A·II. Slurry.

Formulation				
Active material	Conductive additives	CMC	Second binder	pH
88 wt.-% D-PW	6 wt.-%	2 wt.-%	4 wt.-% TRD	9.9
88 wt.-% H-PW	6 wt.-%	2 wt.-%	4 wt.-% TRD	7.9
90 wt.-% H-PW	4 wt.-%	2 wt.-%	4 wt.-% TRD	7.3
90 wt.-% H-PW	4 wt.-%	2 wt.-%	4 wt.-% PAA	6.4
90 wt.-% H-PW	4 wt.-%	2 wt.-%	4 wt.-% LA132	7.8
90 wt.-% H-PW	4 wt.-%	2 wt.-%	4 wt.-% LA133	7.1
90 wt.-% LFP	4 wt.-%	2 wt.-%	4 wt.-% LA133	9.2

Note: The conductive additives and CMC are not specified in this table. The information can be found in the part Experimental.

Table A·III. Fitting parameters of full cells based on the data obtained from impedance measurements.

Sample	Cell D			Cell H		
	Initial	100 cycles	200 cycles	Initial	100 cycles	200 cycles
R_Ω (Ω)	9.25 ± 0.01	7.60 ± 0.04	7.21 ± 0.04	3.74 ± 0.01	3.59 ± 0.02	3.55 ± 0.01
R_{SF} (Ω)	1.90 ± 0.02	1.26 ± 0.05	1.75 ± 0.05	1.54 ± 0.01	1.17 ± 0.02	3.45 ± 0.03
Q_1 (10^{-4} $\Omega^{-1}s^{\alpha 1}$)	4.1 ± 0.1	1.3 ± 0.1	2.0 ± 0.2	4.7 ± 0.1	1.4 ± 0.1	2.30 ± 0.03
α_1	0.700	0.789	0.735	0.713	0.815	0.761
R_{ct} (Ω)	14.7 ± 0.6	94 ± 1	123 ± 2	162 ± 2	127 ± 1	132 ± 1
Q_2 (10^{-4} $\Omega^{-1}s^{\alpha 2}$)	4.1 ± 0.5	7.06 ± 0.01	10.0 ± 0.1	5.75 ± 0.01	7.53 ± 0.03	1.3 ± 0.1
α_2	0.897	0.762	0.701	0.820	0.760	0.722
δ_W (Ω $s^{-1/2}$)	425 ± 1	125 ± 3	83 ± 5	545 ± 3	16 ± 3	17 ± 2

Table A·IV. Comparison of electrodes composed of C65, CMC and a second binder without active material.

Second binder	Water content (10^3 ppm)
TRD	15
PAA	98
LA132	20
LA133	22

The coating was made with the mass ratio of conductive additive to polymeric binders of 4:6 and stored 24 h in humid air (100% relative humidity, 25 °C) before the water content was determined by means of Karl Fischer titration on a coulometric titration device (Titrator Compact C30SD, Mettler-Toledo).

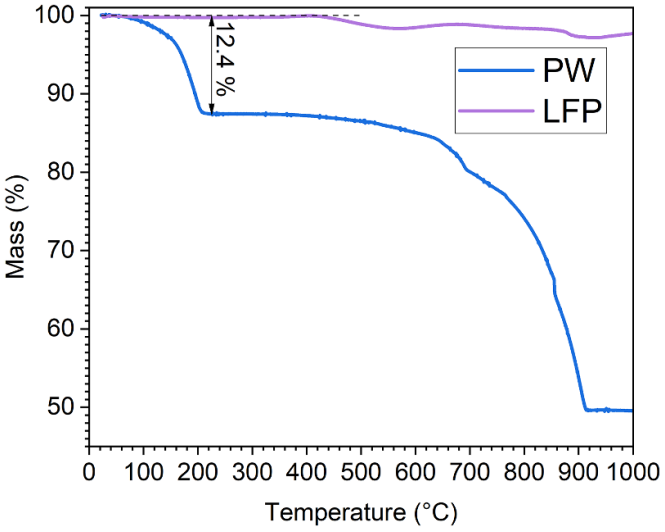

Figure A·1. TGA results of as received PW and LFP for a temperature of 25 °C to 1000 °C with a heating rate of 5 K min^{-1}. The loss of water for PW sample is indicated and results in a relative weight loss of 12.4 wt.-%.

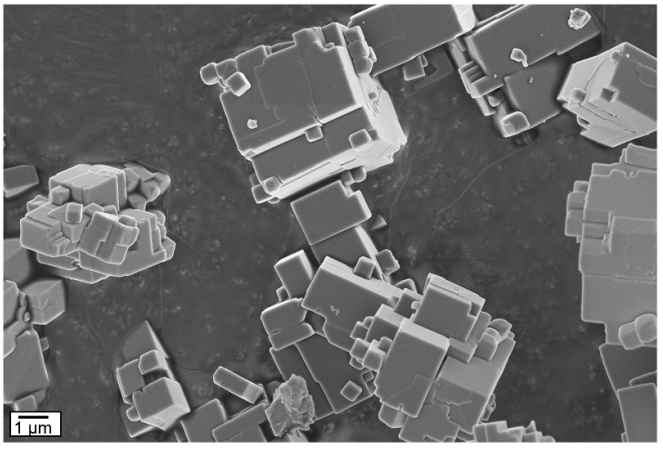

Figure A·2. SEM micrographs of as-received PW.

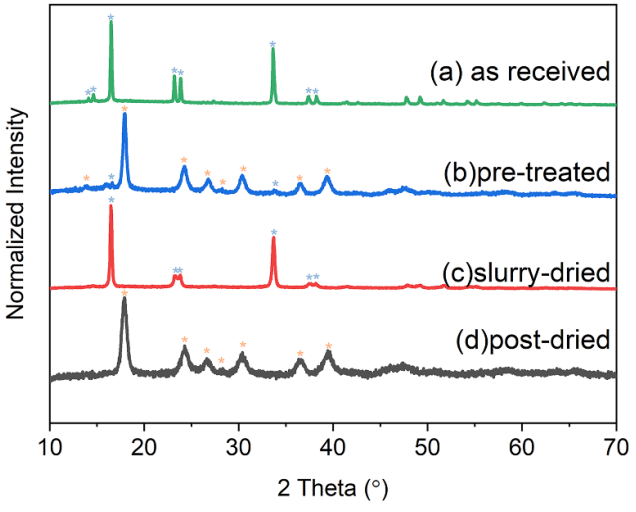

Figure A·3. XRD results of D-PW at different time-frames in the manufacturing procedure: (a) as received (b) pre-treated (c) rehydrated & dried (d) post-dried. (reflections of rhombohedral and monoclinic phases between 10° and 40° are marked with orange and blue, respectively, according to the XRD pattern reported by Song et al. [11]).

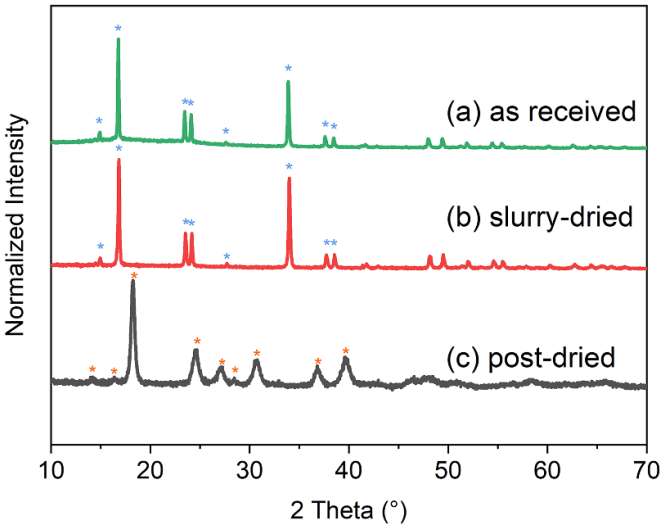

Figure A·4. XRD results of H-PW at different time-frames in the manufacturing procedure: (a) as received (b) hydrated & dried (c) post-dried. (reflections of rhombohedral and monoclinic phases between 10° and 40 ° are marked with orange and blue, respectively, according to the XRD pattern reported by Song et al.[11]).

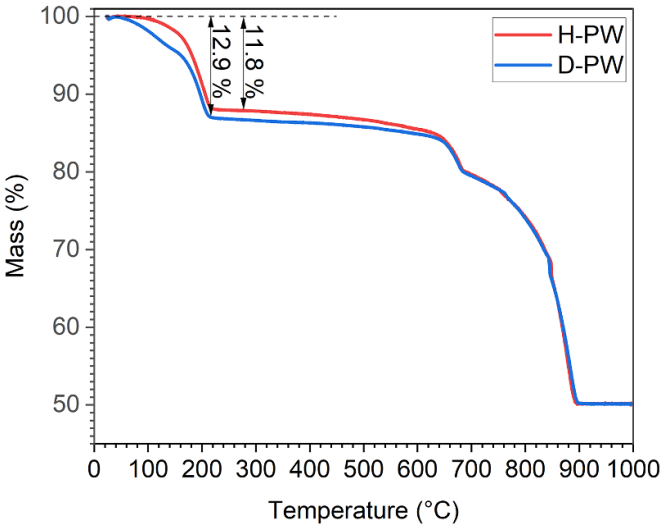

Figure A·5. TGA results of water-washed H-PW and D-PW measured between 25 °C and 1000 °C with a heating rate of 5 K min^{-1}. The loss of water is indicated and results in a relative weight loss of 11.8 wt.-% (H-PW washed with water) and 12.9 wt.-% (D-PW washed with water), respectively.

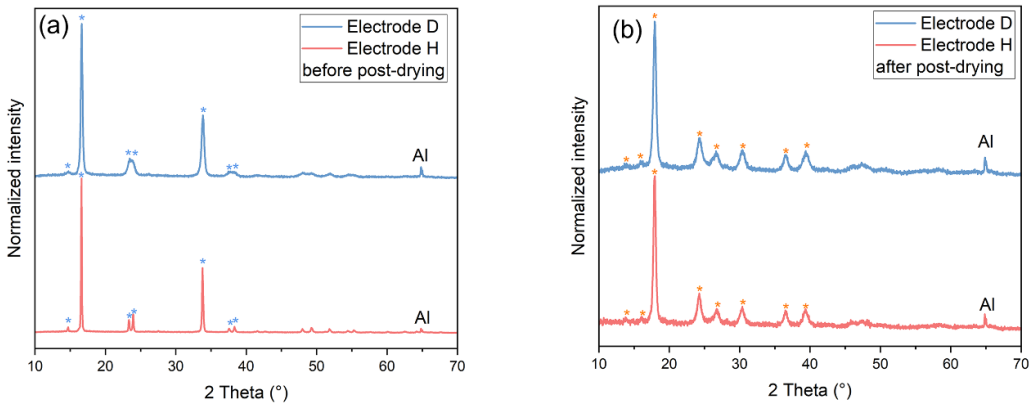

Figure A·6. XRD results of electrode D and electrode H before and after post-drying (reflections of rhombohedral and monoclinic phases between 10° and 40 ° are marked with orange and blue, respectively, according to the XRD pattern reported by Song et al.[11]). Due to presence of aluminum foil, a reflection is detected at a $2\theta = 65°$ according to Xu et al.[48]

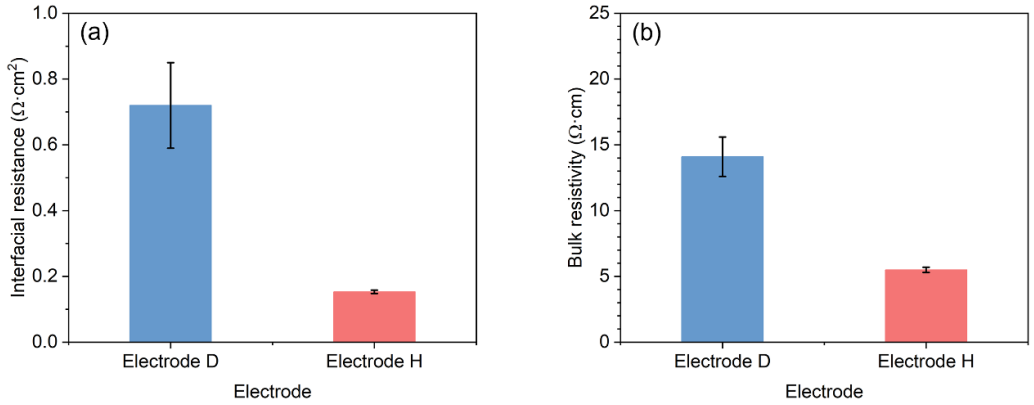

Figure A·7. Comparison between electrode D and H in terms of (a) interfacial resistance and (b) bulk resistivity measured after post-drying.

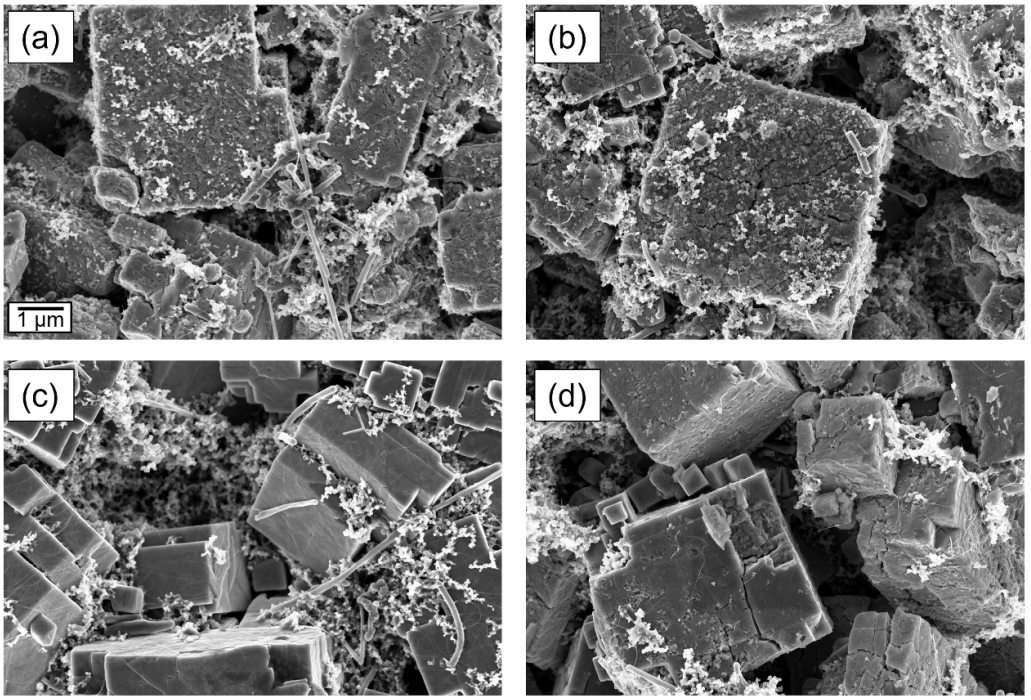

Figure A·8. SEM micrographs of PW electrodes: (a) electrode D, before cycling; (b) electrode D, after cycling; (c) electrode H, before cycling; (d) electrode H, after cycling.

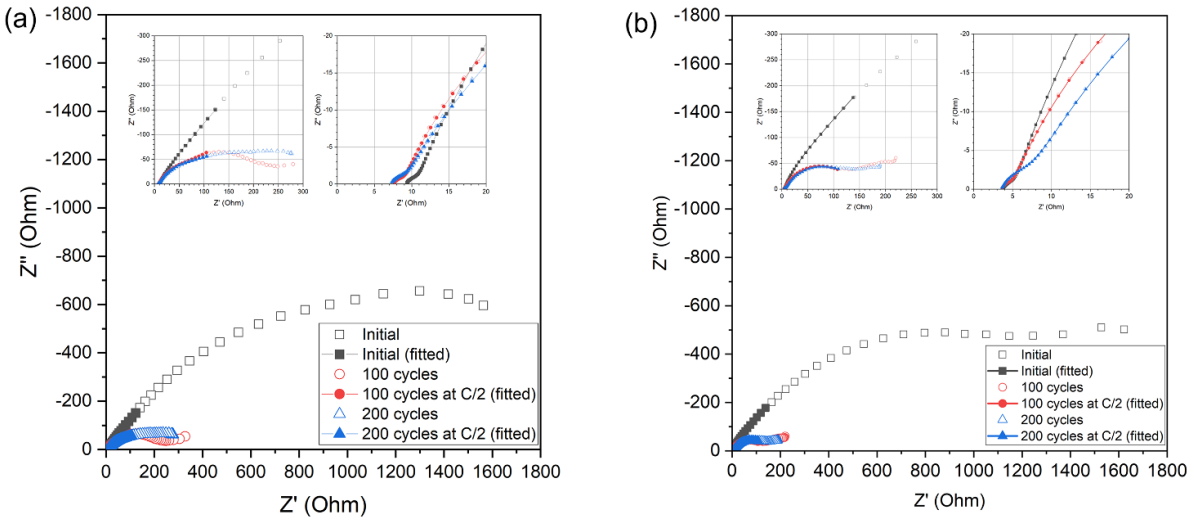

Figure A·9. Impedance measurements of (a) cell D and (b) cell H after formation cycles and after cycling at C/2 presented in Nyquist plots. Fitting is conducted according to the equivalent circuit presented in Fig. A·11c between 1 Hz and 100 kHz.

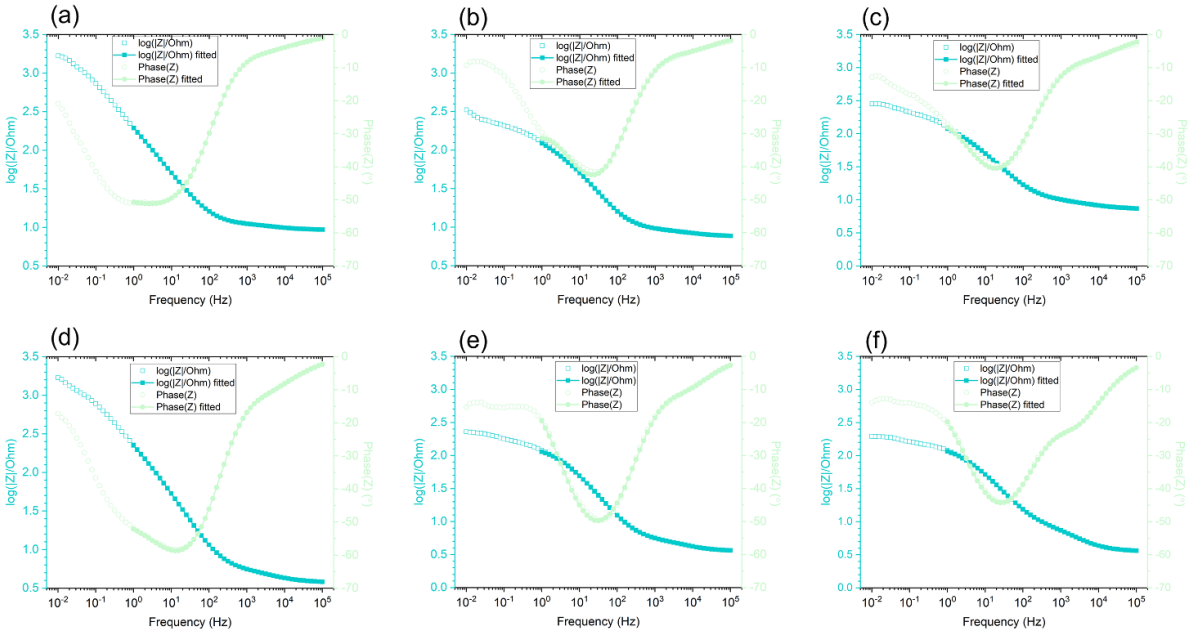

Figure A·10. Impedance measurements of cell D and cell H after formation cycles and after cycling at C/2 presented in Bode plots: (a) cell D after two formation cycles at C/20, (b) cell D after cycling at C/2 for 100 cycles, (c) cell D after cycling at C/2 for 200 cycles, (d) cell H after two formation cycles at C/20, (e) cell H after cycling at C/2 for 100 cycles, (f) cell H after cycling at C/2 for 200 cycles. Fitting is conducted according to the equivalent circuit presented in Fig. A·11c between 1 Hz and 100 kHz.

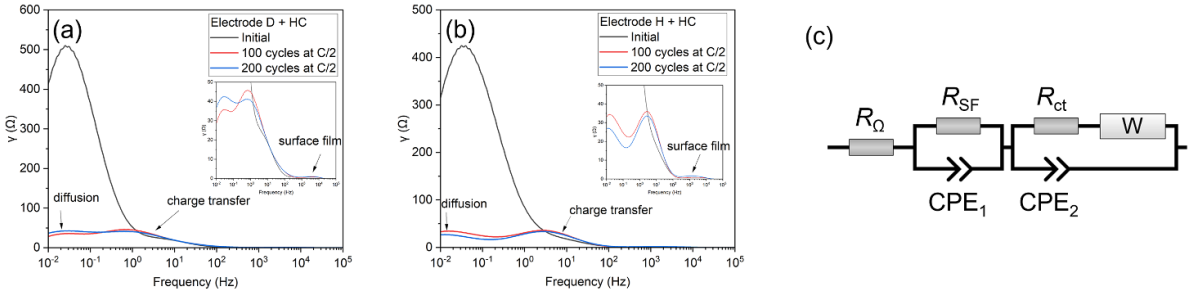

Figure A·11. DRT analysis of (a) cell D and (b) cell H as well as (c) their corresponding equivalent circuit.

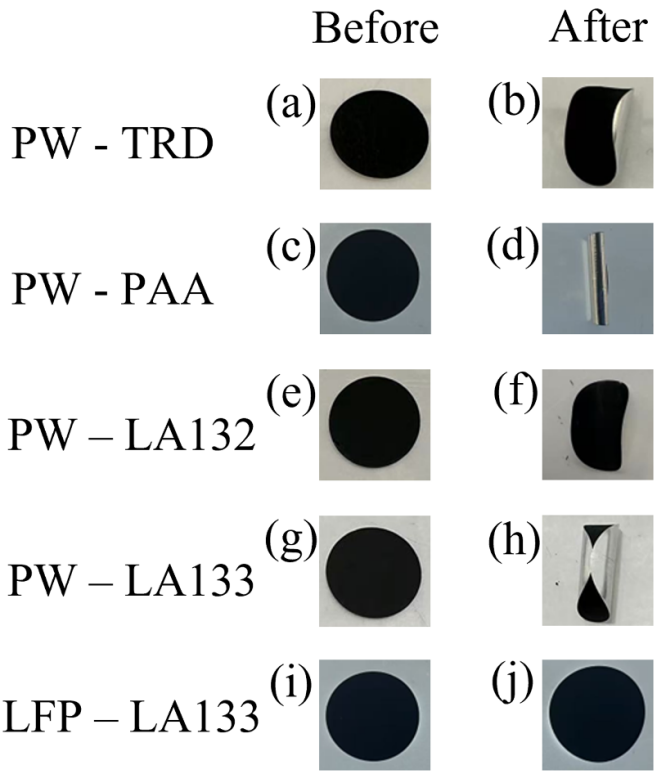

Figure A·12. Comparison of electrodes (16 mm in diameter) composed of PW or LFP with conductive additive C65 and various binder combinations before and after post-drying: (a) CMC/TRD, before post drying; (b) CMC/TRD, after post drying; (c) CMC/PAA, before post drying; (d) CMC/PAA, after post drying; (e) CMC/LA132, before post drying; (f) CMC/LA132, after post drying; (g) CMC/LA133, before post drying; (h) CMC/LA133, after post drying; (i) CMC/LA132, before post drying and (j) CMC/LA132, after post drying. The active material for electrode a–h is PW and the active material for electrodes i and j is LFP.

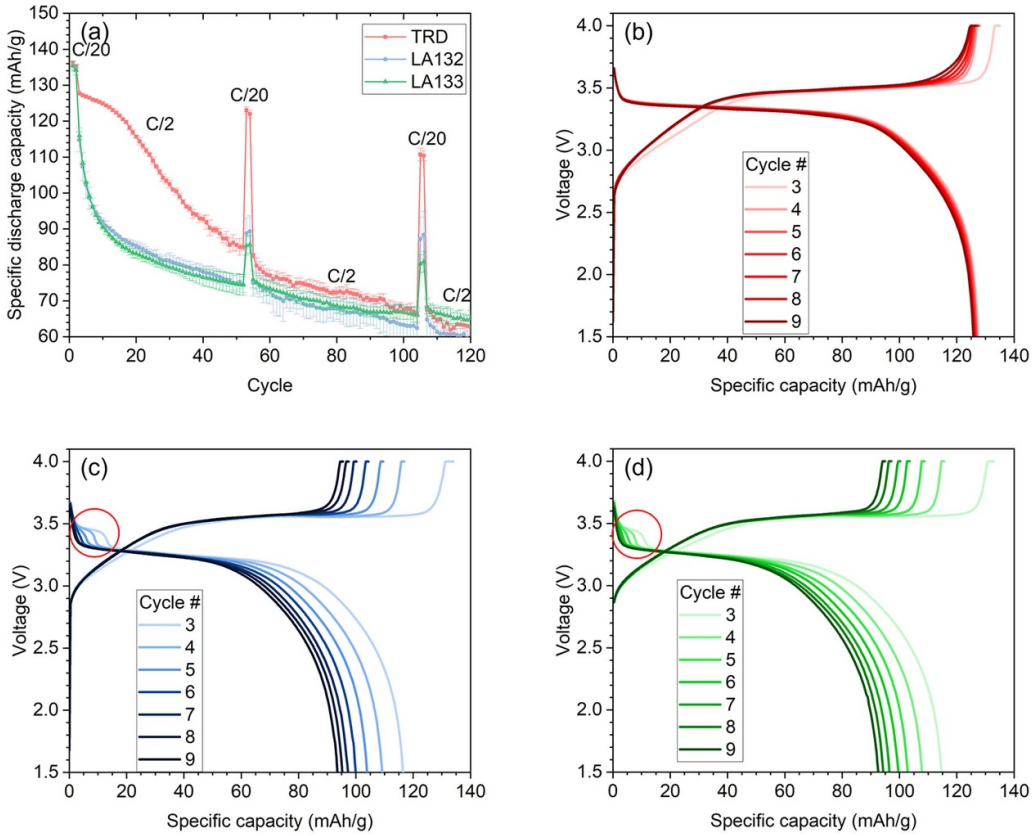

Figure A·13. Electrochemical performance of electrodes with TRD, LA132 or LA133 (for trials of optimizing mechanical properties) in the first 120 cycles: (a) long term cycling performance; (b) charge and discharge curves of TRD-based electrode between Cycle 3 and 9; (c) charge and discharge curves of LA132-based electrode between Cycle 3 and 9; (d) charge and discharge curves of LA133-based electrode between Cycle 3 and 9. Note: The data from one representative cell of each electrode were selected for the charge and discharge curves presented in (b)–(d). The additional plateau at around 3.45 V is circled in (c) and (d).

ORCID

Xuebin Wu https://orcid.org/0009-0004-8810-6682
Noah Keim https://orcid.org/0000-0002-3338-5811
David Burger https://orcid.org/0009-0000-9070-9395
Haofei Zhou https://orcid.org/0009-0008-4954-8604
Dhruvil Virani https://orcid.org/0009-0007-1723-6369
Marcus Müller https://orcid.org/0000-0002-5562-7201
Ulrike Kaufmann https://orcid.org/0009-0001-1287-4982
Joachim R. Binder https://orcid.org/0000-0003-2237-1411
Philip Scharfer https://orcid.org/0000-0003-1243-460X
Wilhelm Schabel https://orcid.org/0000-0002-3453-8242
Helmut Ehrenberg https://orcid.org/0000-0002-5134-7130
Werner Bauer https://orcid.org/0000-0002-5923-2426

References

1. J. B. Goodenough and Y. Kim, *Chem. Mater.*, **22**, 587 (2010).
2. Z. Yang, J. Zhang, M. C. W. Kintner-meyer, X. Lu, D. Choi, J. P. Lemmon and J. Liu, *Chem. Rev.*, **111**, 3577 (2011).
3. D. Bresser, D. Buchholz, A. Moretti, A. Varzi and S. Passerini, *Energy Environ. Sci.*, **11**, 3096 (2018).
4. D. L. Wood, J. D. Quass, J. Li, S. Ahmed, D. Ventola and C. Daniel, *Dry. Technol.*, **36**, 234 (2018).
5. S. Ahmed, P. A. Nelson, K. G. Gallagher and D. W. Dees, *J. Power Sources*, **322**, 169 (2016).
6. W. Zuo et al., *Nat. Commun.*, **11**, 3544 (2020).
7. D. O. Ojwang, M. Svensson, C. Njel, R. Mogensen, A. S. Menon, T. Ericsson, L. Häggström, J. Maibach and W. R. Brant, *ACS Appl. Mater. Interfaces*, **13**, 10054 (2021).
8. I. Doberdò, N. Löffler, N. Laszczynski, D. Cericola, N. Penazzi, S. Bodoardo, G.-T. Kim and S. Passerini, *J. Power Sources*, **248**, 1000 (2014).
9. W. Bauer, F. A. Çetinel, M. Müller and U. Kaufmann, *Electrochim. Acta*, **317**, 112 (2019).
10. C.-C. Li, J.-T. Lee, Y.-L. Tung and C.-R. Yang, *J. Mater. Sci.*, **42**, 5773 (2007).
11. J. Song, L. Wang, Y. Lu, J. Liu, B. Guo, P. Xiao, J.-J. Lee, X.-Q. Yang, G. Henkelman and J. B. Goodenough, *J. Am. Chem. Soc.*, **137**, 2658 (2015).
12. L. Ge et al., *ACS Nano*, **18**, 3542 (2024).
13. S. Ali et al., *Electrochim. Acta*, **521**, 145920 (2025).
14. A. Clavelin, D. L. Thanh, I. Bobrikov, M. Fehse, N. E. Drewett, G. A. López, D. Saurel and M. Galceran, *ACS Mater. Lett.*, **6**, 5208 (2024).
15. L. Hartmann, J. Deshmukh, L. Zhang, S. Buechele and M. Metzger, *J. Electrochem. Soc.*, **170**, 030540 (2023).
16. J. Luo et al., *Small*, **21**, e08344 (2025).
17. W. Wang et al., *Adv. Funct. Mater.*, **32**, 2111727 (2022).
18. Z. Li, Y. Wang, F. Rabuel, M. Deschamps, G. Rousse, O. Sel and J.-M. Tarascon, *Energy Storage Mater.*, **76**, 104118 (2025).
19. G. Wang et al., *ACS Nano*, **19**, 22093 (2025).
20. S. Büchele et al., *Batter. Supercaps*, **8**, e202500015 (2025).
21. F. M. Maddar, D. Walker, T. W. Chamberlain, J. Compton, A. S. Menon, M. Copley and I. Hasa, *J. Mater. Chem. A*, **11**, 15778 (2023).
22. S. Roberts, L. Chen, B. Kishore, C. E. J. Dancer, M. J. H. Simmons and E. Kendrick, *J. Colloid Interface Sci.*, **627**, 427 (2022).
23. P. Stüble, C. Müller, J. Klemens, P. Scharfer, W. Schabel, M. Häringer, J. R. Binder, A. Hofmann and A. Smith, *Batter. Supercaps*, **7**, e202300375 (2024).
24. I. Nielsen, D. Dzodan, D. O. Ojwang, P. F. Henry, A. Ulander, G. Ek, L. Häggström, T. Ericsson, H. L. B. Boström and W. R. Brant, *J. Phys. Energy*, **4**, 044012 (2022).
25. N. Y. Samoylova, I. A. Bobrikov, I. Razanau, S. V. Sumnikov, R. N. Vasin, E. A. Korneeva, O. Y. Ponomareva and U. Novikau, *J. Alloys Compd.*, **983**, 173849 (2024).
26. J. Qian, M. Zhou, Y. Cao, X. Ai and H. Yang, *Adv. Energy Mater.*, **2**, 410 (2012).
27. W. Tang, Y. Xie, F. Peng, Y. Yang, F. Feng, X.-Z. Liao, Y.-S. He, Z.-F. Ma, Z. Chen and Y. Ren, *J. Electrochem. Soc.*, **165**, A3910–A7 (2018).
28. Y. Su, Q. Zhang, L. Chen, L. Bao, Y. Lu, Q. Shi, J. Wang, S. Chen and F. Wu, *ChemSusChem*, **13**, 426 (2020).
29. W. An, B. Gao, S. Mei, B. Xiang, J. Fu, L. Wang, Q. Zhang, P. K. Chu and K. Huo, *Nat. Commun.*, **10**, 1447 (2019).
30. Y. Luo, J. Shen, Y. Yao, J. Dai, F. Ling, L. Li, Y. Jiang, X. Wu, X. Rui and Y. Yu, *Adv. Mater.*, **36**, 2405458 (2024).
31. Q. Han, Z. Yang, Y. Hu, S. Gao, X. Liu, C. Wang and J. Han, *Chem. Eng. J.*, **493**, 152575 (2024).
32. J. Sterzinger, R. Streng, S. Chen, R. Götz, W. Hu, J. Li and A. S. Bandarenka, *J. Phys. Chem. C*, **129**, 7135 (2025).

33. X. Chen, L. Li, M. Liu, T. Huang and A. Yu, *J. Power Sources*, **496**, 229867 (2021).
34. A. C. Lazanas and M. I. Prodromidis, *ACS Meas. Sci. Au*, **3**, 162 (2023).
35. S. D. Talian, S. Brutti, M. A. Navarra, J. Moškon and M. Gaberscek, *Energy Storage Mater.*, **69**, 103413 (2024).
36. W. Porcher, P. Moreau, B. Lestriez, S. Jouanneau, F. Le Cras and D. Guyomard, *Ionics*, **14**, 583 (2008).
37. A. Weber, N. Keim, P. Koch, M. Müller, W. Bauer and H. Ehrenberg, *Sci. Rep.*, **15**, 10024 (2025).
38. F. Huttner, W. Haselrieder and A. Kwade, *Energy Technol.*, **8**, 1900245 (2020).
39. Y. Ma, J. Ma and G. Cui, *Energy Storage Mater.*, **20**, 146 (2019).
40. A. Goswami, G. Adithya, H. V. S. R. M. Koppisetti and A. Mukhopadhyay, *J. Power Sources*, **678**, 240105 (2026).
41. B. Erman and P. J. Flory, *Macromolecules*, **19**, 2342 (1986).
42. S. Eichler, O. Ramon, I. Ladyzhinski, Y. Cohen and S. Mizrahi, *Food Res. Int.*, **30**, 719 (1997).
43. H. Wang, D. Wei, Z. Wan, Q. Du, B. Zhang, M. Ling and C. Liang, *Electrochim. Acta*, **368**, 137580 (2021).
44. L. Gong, M. H. T. Nguyen and E.-S. Oh, *Electrochem. Commun.*, **29**, 45 (2013).
45. L. Luo, Y. Xu, H. Zhang, X. Han, H. Dong, X. Xu, C. Chen, Y. Zhang and J. Lin, *ACS Appl. Mater. Interfaces*, **8**, 8154 (2016).
46. H. Zhong, M. Sun, Y. Li, J. He, J. Yang and L. Zhang, *J. Solid State Electrochem.*, **20**, 1 (2016).
47. W. Wang, X. Yue, J. Meng, X. Wang, Y. Zhou, Q. Wang and Z. Fu, *J. Phys. Chem. C*, **123**, 250 (2019).
48. X. Xu, Z. Liu, B. Zhang, H. Chen, J. Zhang, T. Wang, K. Zhang, J. Zhang and P. Huang, *Appl. Phys. A*, **125**, 490 (2019).